

# Research on the Non-uniform Flow Characteristics in a Screw Mixed-flow Deep-sea Mining Pump

D. Ma<sup>1</sup>, Z. Shen<sup>1,2</sup>, W. Yang<sup>1</sup>, F. Jiang<sup>1</sup>, and R. Li<sup>†1,2</sup>

<sup>1</sup> School of Energy and Power Engineering, Lanzhou University of Technology, Lanzhou, Gansu, China

<sup>2</sup> Key Laboratory of Fluid Machinery and Systems of Gansu Province, Lanzhou Gansu, China

†Corresponding Author Email: [lirn@lut.edu.cn](mailto:lirn@lut.edu.cn)

## ABSTRACT

Deep-sea slurry pump is a crucial component for achieving vertical transportation of ore particles in pump-pipe lifting deep-sea mining systems. However, traditional mining pump structures face challenges, such as insufficient particle flow capacity and blockage susceptibility, which affect the slurry pump's operational stability. This study introduces a novel deep-sea slurry pump design that incorporates the non-clogging structural characteristics of a screw mixed flow impeller combined with a diffuser. The pump flow capacity was evaluated using the CFD-DEM (Computational Fluid Dynamics - Discrete Element Method) coupling method for transporting 10 mm spherical particles at various flow rates. The motion patterns and non-uniform distribution characteristics of particles were analyzed qualitatively and quantitatively within the pump under different inflow conditions. The proposed pump demonstrated a robust coarse particle overflow capacity for varying particle transport states and unequal particle distribution among flow components. The particle quantity changed consistently throughout the transportation process and was divided into a growth phase and a stable phase. The main flow components exhibited a dynamic non-uniform particle flow with a more pronounced periodic nature in the impeller channel. The degree of non-uniform particle flow in the diffuser channel was inversely related to the flow rate, and was higher compared to the impeller channel.

## Article History

Received October 9, 2024

Revised January 23, 2025

Accepted February 13, 2025

Available online May 5, 2025

## Keywords:

CFD-DEM

Deep-sea mining pump

Screw mixed flow pump

Solid-liquid two-phase flow

Non-uniform flow

Numerical simulation

## 1. INTRODUCTION

Mineral resources are fundamental to the advancement of human society. Diverse polymetallic nodules in the deep sea, characterized by their vast reserves and high quality, are essential raw materials for modern high-tech industries, advanced equipment manufacturing, and emerging technologies (Zhu et al., 2024). In recent decades, numerous countries have intensified their efforts to explore and exploit marine mineral resources (Yang et al., 2020; Wang et al., 2023; Zou et al., 2023). The mining pump is a critical component of deep-sea metal nodule mining systems, distinct from pumps used for pure fluids (Dehghan & Shojaeefard, 2022; Dehghan et al., 2024). It consists of a multi-stage pump with a mixed-flow impeller and diffuser (Fig. 1). KSB Co. Ltd, Germany, developed the first deep-sea mining pump; however, it faced operational issues, such as wear and difficulties in replacing worn parts (Kuntz, 1979). Subsequent pumps developed in Japan (Tram, 1991) and South Korea (Cundall & Hart, 1985) encountered varying degrees of

local particle clogging. A deep-sea mining pump developed in China incorporated amplified flow to the hydraulic design of the impeller to meet the requirements of an impeller outlet width of thrice the maximum particle size, aiming to enhance the overflow capacity of coarse particles in the flow channel (Yang et al. 2014; Yang & Liu 2020; Zou et al., 2021). Nevertheless, this setup experienced flow channel clogging issues during testing (Wang et al., 2021).

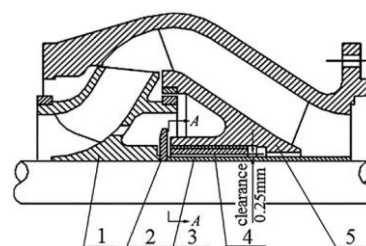
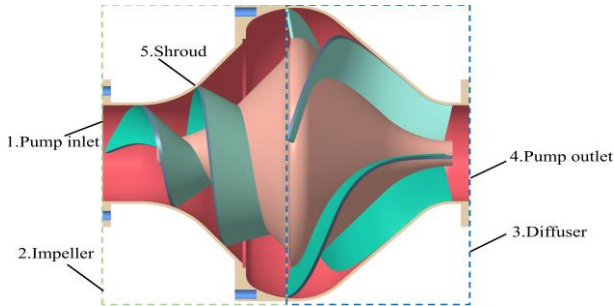


Fig 1 Deep-sea lift pump with bowl diffuser: (1) Impeller, (2) sand tray, (3) shaft sleeve, (4) bearing, (5) diffuser (Kang et al., 2019)

NOMENCLATURE			
$D_1$	impeller inlet diameter	$H$	head
$D_2$	impeller average outlet diameter	$\alpha_1$	diffuser inlet blade angle
$b_2$	blade outlet width	$\alpha_2$	diffuser outlet blade angle
$\beta_2$	outlet blade angle	$Q$	flow rate
$D_3$	diffuser maximum diameter of the internal streamline	$n$	revolution per minutes
$D_4$	diffuser maximum diameter of the external streamline	$C_v$	volume fraction of transported particles
$Z_2$	diffuser number of blades	$\varphi$	particle non-uniformity



**Fig. 2 Model pump geometry**

In recent years, advancements in computational fluid dynamics (CFD) have led to the increased application of CFD – discrete element method (DEM) coupling to deep-sea mining pump research. Studies have analyzed the influence of pump rotational speed, particle volume fraction, flow rate, and other parameters on the particle flow capacity in deep-sea mining pumps through experiments and numerical simulations (Yang et al.2017; Zou et al., 2019; Guan et al., 2021; Hu et al., 2021). Ding et al. (2021) investigated a two-stage slurry pump, revealing particle aggregation in the impeller and spatial guide vane through numerical calculations. While this aggregation did not affect slurry permeability, it caused flow loss and component wear. Su et al. (2020) conducted experiments and numerical simulations on a two-stage deep-sea mining pump, revealing an unequal particle distribution between the first- and second-stage pumps, with particles prone to deposition at the pump inlet. Deng et al. (2021) examined the movement of coarse particles in a six-stage lifting pump and concluded that particle movement in each pump stage can be divided into three phases, with uneven particle distribution across stages. Wang et al. (2021) observed that larger particles are more likely to aggregate within a single-stage mining pump.

Screw mixed-flow impellers are renowned for their exceptional anti-clogging capabilities and geometric advantages, particularly their large outlet width (Shen & Chu, 2018; Shen et al., 2018). These impellers are extensively utilized in the transportation of two-phase flows containing substantial solids and fibrous materials. This paper introduces a novel structure combining a screw mixed-flow impeller and diffuser with a screw open-flow channel. The proposed design incorporates a semi-open impeller and shroud, enhancing the particle overflow capacity within the impeller.

This study employs the CFD-DEM coupling approach to investigate the kinematic and dynamic behavior of

**Table 1 Structural parameters of screw mixed-sea mining pump**

Item	Parameter	Value
Impeller	Inlet diameter $D_1$	208 mm
	Average outlet diameter $D_2$	492 mm
	Blade outlet width $b_2$	77 mm
	Outlet blade angle $\beta_2$	15°
	Specific speed $n_s$	106
	Scroll of blade	725
Diffuser	Blade tip clearance	1 mm
	Maximum diameter of the internal streamline $D_3$	500 mm
	Maximum diameter of the external streamline $D_4$	628 mm
	Number of blades $Z_2$	4
	Inlet blade angle $\alpha_1$	16°
	Outlet blade angle $\alpha_2$	90°

particles within a pump. The flow structure, particle movement patterns, and distribution characteristics of slurry, comprising fluid, and coarse ore particles, were analyzed under various flow boundary conditions. This study aims to provide a theoretical foundation for the design and optimization of future deep-sea mining pump development.

## 2. MODEL PARAMETERS AND ANALYSIS METHODS

### 2.1 Fluid Domain Modeling and Meshing

The fundamental design parameters of the model pump included a flow rate of  $Q = 420 \text{ m}^3/\text{h}$ , a head of  $H = 45 \text{ m}$ , and a rotational speed of  $n = 1480 \text{ rpm}$  (structural parameters presented in Table 1). Figure 2 illustrates the geometric configuration of the screw mixed flow deep sea mining pump.

Fluent meshing was employed to perform polyhedral meshing of the inlet pipe, impeller flow channel, diffuser flow channel, and outlet pipe of the pump. The pump was positioned vertically with the fluid and particle inlets at the bottom. The mesh near the top gap was refined to better capture the flow, considering the influence of the jet caused by top gap leakage on particle motion within the pump. To ensure accurate numerical calculations, five grid schemes with varying resolutions were established. The grid scheme applicability was verified by utilizing the head change as an indicator to assess grid independence (Table 2).

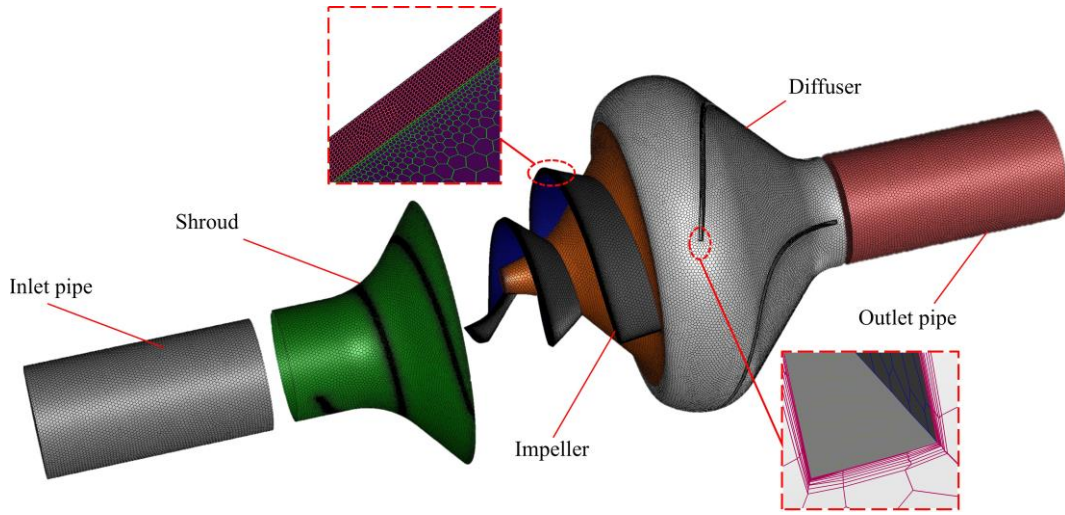


**Fig. 3 Three-dimensional grid model of screw mixed-flow deep-sea mining pump**

**Table 2 Mesh independence check**

Item	Number of Mesh	Head/m	Head Change Rate/%
No. 1	452,504	52.57	3.91
No. 2	1,112,837	52.21	4.63
No. 3	1,861,334	54.63	0
No. 4	2,349,998	55.05	-0.76
No. 5	3,218,106	53.68	1.77

Table 2 shows the change in the pump head under different grid resolutions. It is evident that the pump head change rate remains within 5% when the number of grids exceeds  $1.8 \times 10^6$ . To balance computational resources and accuracy, the NO.3 scheme was selected for subsequent analysis and computation. The meshing details of the scheme are illustrated in Fig. 3.

## 2.2 Model Control Equations

In CFD-DEM coupled computation, the fluid is treated as a continuous incompressible medium governed by the Navier-Stokes continuity and momentum equations (Zou et al., 2020). The particulate system employed Newtonian equations of motion and a contact model to describe the motion of individual particulates. Real-time information exchange between the flow and particulate fields was achieved through user-defined functions (UDFs) in the coupled computation process.

The fluid continuity equation is expressed as:

$$\frac{\partial \varepsilon \rho}{\partial t} + \nabla \cdot \rho \varepsilon u = 0 \quad (1)$$

Where:  $\rho$  is the fluid density;  $t$  is the time;  $u$  is the fluid velocity;  $\varepsilon$  is the fluid volume fraction.

The fluid momentum conservation equation is expressed as:

$$\begin{aligned} \frac{\partial \varepsilon \rho u}{\partial t} + \nabla \cdot \rho \varepsilon \mu u = & -\nabla \rho + \nabla \cdot (\mu \varepsilon \nabla u) \\ & + \rho \varepsilon g - S \end{aligned} \quad (2)$$

Where:  $g$  is the gravitational acceleration;  $\mu$  is the fluid viscosity;  $S$  is the momentum sink generated by the relative motion between the solid-liquid and the liquid phases, thus realizing the coupling between the fluid phase and the particle phase. The momentum sink is calculated by equation (3):

$$S = \frac{\sum_i^n F_D}{V} \quad (3)$$

Where:  $F$  is the fluid resistance in the grid cell, and  $V$  is the grid cell volume.

During the mining conveying process, according to the particle force-displacement relationship, the force it is subjected to can be obtained from the particle displacement (Weaver & Mišković, 2024), and the equations of motion of the particles are calculated by (4) and (5):

$$\begin{aligned} m_p \frac{dv_p}{dt} = & f_{d,i} + f_{\nabla p,i} + f_{\nabla \tau,i} + f_{Ar,i} + f_{vm,i} \\ & + f_{Saff,i} + f_{Mag,i} + f_{g,i} + f_{c,i} \end{aligned} \quad (4)$$

$$I_p \frac{dw_p}{dt} = M_p \quad (5)$$

where  $m_p$ ,  $I_p$ ,  $v_p$ , and  $w_p$  are the particle's mass, momentum, translational velocity, and rotational velocity, respectively;  $f_{d,i}$  is the fluid trailing force on the particle;  $f_{\nabla p,i}$  is the pressure gradient force on the particle in the flow field;  $f_{\nabla \tau,i}$  is the viscous drag;  $f_{Ar,i}$  is the buoyancy force on the particle;  $f_{vm,i}$  is the virtual mass force;  $f_{Saff,i}$  is the Saffman lift generated by the particle subjected to fluid shear;  $f_{Mag,i}$  is the Magnus lift generated by the particle spinning in the flow field;  $f_{g,i}$  is the gravitational force of the particle; and  $f_{c,i}$  is the sum of the normal and tangential forces acting on the particle post-collision.

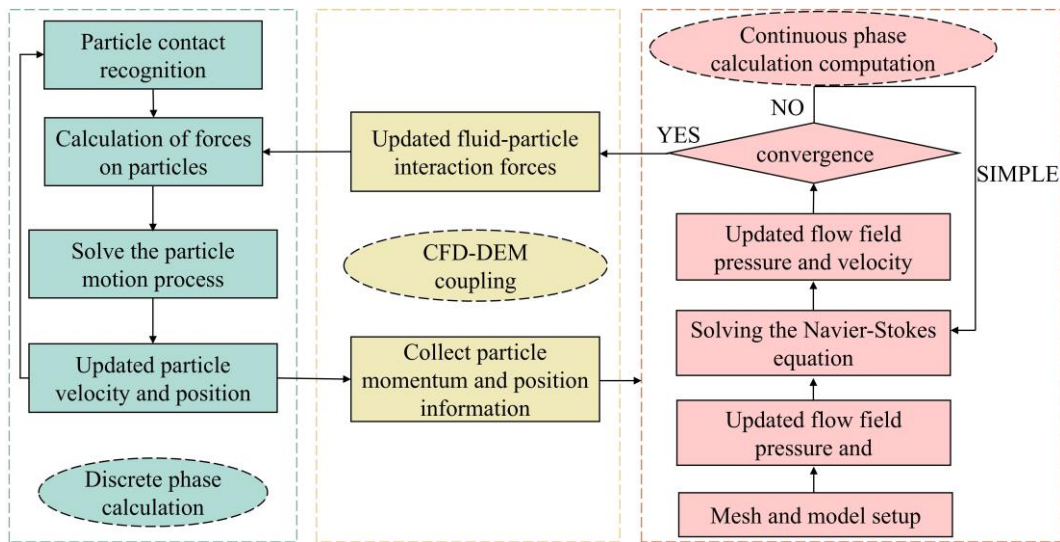


Fig. 4 CFD-DEM coupled calculation workflow

The Fluent and EDEM commercial computational software were employed to construct a coupled computational platform (Fig. 4). The steps for coupling calculation are as follows, first, the continuous phase was resolved using Fluent. After the calculation is iterated until convergence, the flow field data is transferred to EDEM. Based on the flow field data, the particle motion state was calculated, and the original particle position and velocity were updated. Then, the particle motion information is returned to the continuous phase solver, and the calculation proceeds iteratively to the next computational time step until the calculation is completed (Wang et al., 2024).

### 2.3 CFD-DEM Coupled Computational Strategy

During operation, deep-sea mining pumps encounter extremely challenging environments, influenced by various factors, such as ocean currents, internal waves, and water depth. These conditions can lead to system flow fluctuations, necessitating a study of the pump's overflow capacity for coarse particles under multiple operating conditions. Through CFD-DEM coupled simulation, this study elucidates the particle motion patterns and distribution characteristics within the pump for a transported particle volume fraction of  $C_v = 5\%$ .

The liquid phase was considered the continuous phase, while the particles were treated as the discrete phase. The coarse particles were assumed to be spherical with a diameter of 10 mm. The calculation time was determined based on the convergence of residuals under different flow rates and the particle motion conditions within the pump. Data from the last 10 operational cycles were selected for analysis after the number of particles in the pump reached a steady state. The RNG  $k-\epsilon$  turbulence model was employed to account for the presence of vortices and whirlpools in the pump, as it is more suitable for strong rotation and vortex flows (Yakhot & Orszag 1986). The  $Y^+$  wall of the impeller and diffuser was maintained below 100, as per the turbulence model requirements. The standard wall function was utilized to address near-wall high-Reynolds number turbulence issues, while the SIMPLE method was applied for pressure-velocity coupling in the flow field. Furthermore, the convergence

accuracy of residuals for each solution variable was controlled within  $10^{-4}$ .

In the Fluent software, the model pump's inlet was set to a constant velocity, while the outlet was set as a pressure outlet. The interface method is used to complete the data exchange for different geometrical boundaries. The flow in the impeller was computed in the rotating coordinate system, while that in the other components was computed in the stationary coordinate system. In EDEM, the model pump's inlet surface was designated as a dynamic "particle factory," which continuously generated particles with random distributions across the inlet surface; the initial velocity of particles matched that of the fluid. The mass flow rate of the fluid was converted to be the boundary condition of the particle generation rate for different conditions, representing  $C_v=5\%$ , and the particle mass flow rate  $Q_p$  is calculated by equation 6. In the calculation process, the  $Q_p$  at different flow conditions was calculated to be 6.1, 8.9, and 11.7 kg/s. Particles were automatically removed upon reaching the pump's outlet boundary. The Hertz-Mindlin (no slip) model and the standard rolling friction model were used to solve the contact dynamics between particles and walls (Zhou et al., 2019; Table 3 (Ji et al. 2021)). The simulation accounted for the gravitational effect on the fluid, with an acceleration due to gravity of  $g = 9.81 \text{ m/s}^2$ . The particles were set to have a density of  $2000 \text{ kg/m}^3$ , Poisson's ratio of 0.4, and shear modulus of 21.3 Mpa. The pump body is made of iron, with a density of  $7800 \text{ kg/m}^3$ , Poisson's ratio of 0.3, and a shear modulus of 70 Mpa.

Table 3 Particle and wall contact parameters.

Interaction of Object	Particle-particle	Wall-particle
Recovery Factor	0.44	0.5
Coefficient of Static Friction	0.27	0.15
Coefficient of Rolling Friction	0.01	0.01

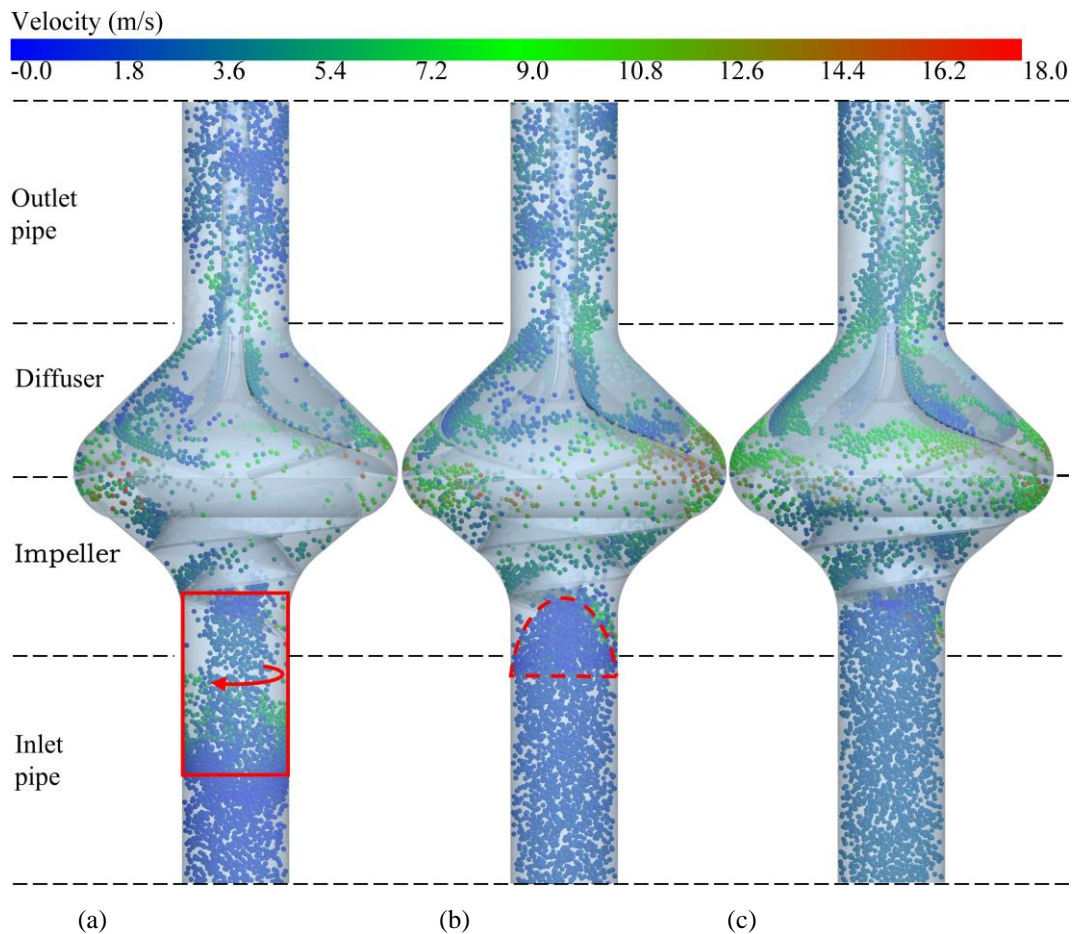


**Fig. 5 Particle distribution in the pump under  $Q =$  (a) 220, (b) 320, and (c) 420  $\text{m}^3/\text{h}$**

$$Q_p = Q_f \times \rho_p \times Cv \quad (6)$$

Where:  $Q_p$  is the particle mass flow rate,  $Q_f$  is the fluid volume flow rate,  $\rho_p$  is the particle density.

The unsteady time step of the flow field was set to  $2.24 \times 10^{-4}$  s, which means that the impeller turns through  $2^\circ$  in one-time step. In the CFD-DEM coupling calculation, the calculation time step in EDEM should be shorter than that in Fluent, and the time step in Fluent maintains a 10 to 100 times relationship with the time step in EDEM. Additionally, the Rayleigh time step in EDEM software was maintained within 10% to 40% of the total time step. Consequently, the EDEM time step was set to  $2.24 \times 10^{-5}$  s, representing 13.86% of the Rayleigh time. This configuration aligned with the principles of the coupled computation.

The duration required for particles within the pump to achieve a stable transport state varied according to the flow conditions, resulting in distinct calculation times. Under a flow rate of 220, 320, and 420  $\text{m}^3/\text{h}$ , the impeller completed 35, 30, and 25 rotations, respectively.

### 3. PARTICLE DISTRIBUTION CHARACTERISTICS

To evaluate the performance of a screw mixed-flow deep-sea mining pump in conveying coarse particles at varying flow rates, it is essential to examine the movement

of particles within the pump. Figure 5 displays the particle distribution characteristics in the pump at various flow rates; at this time, the pump operation time was 1.41s, 1.21s, and 1.01s, respectively. A comparison of particle conveying states across flow rates revealed consistent stability despite changes in pump flow rate. The absence of clogging in the pump channel indicated that the screw mixed-flow impeller-diffuser combination exhibited a high overflow capacity for coarse particles with substantial design redundancy, demonstrating adaptability to external disturbances caused by fluctuations in conveying flow rate. The particle transport state within the pump varied significantly with the flow rate, necessitating a separate analysis of the inlet pipe, impeller channel, diffuser and outlet pipe separately at various flow rates.

#### 3.1 Characteristics of Particle Distribution in the Inlet Pipe

Pump operation under low flow conditions, gravitational effects, fluid prewhirl, wall friction, and other factors resulting from speed reduction led to varying degrees of particle deposition in the inlet pipe (Fig. 5(a) and (b)). Figure 6 shows the velocity streamline distribution in the pump inlet pipe and impeller. The pump operates under low flow conditions, where the fluid and particle inlet velocity are lower than the design conditions. A strong prewhirl was formed in the inlet section due to the high-speed rotation of the impeller. The semi-open

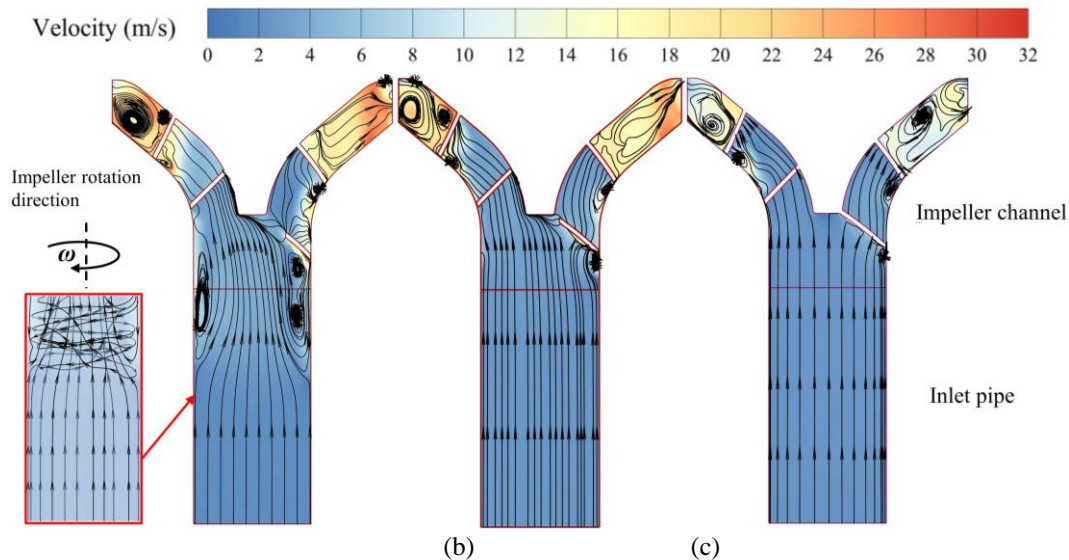


**Fig. 6** Velocity streamlines distribution in the inlet pipe-impeller at  $Q =$  (a) 220, (b) 320, and (c) 420  $\text{m}^3/\text{h}$

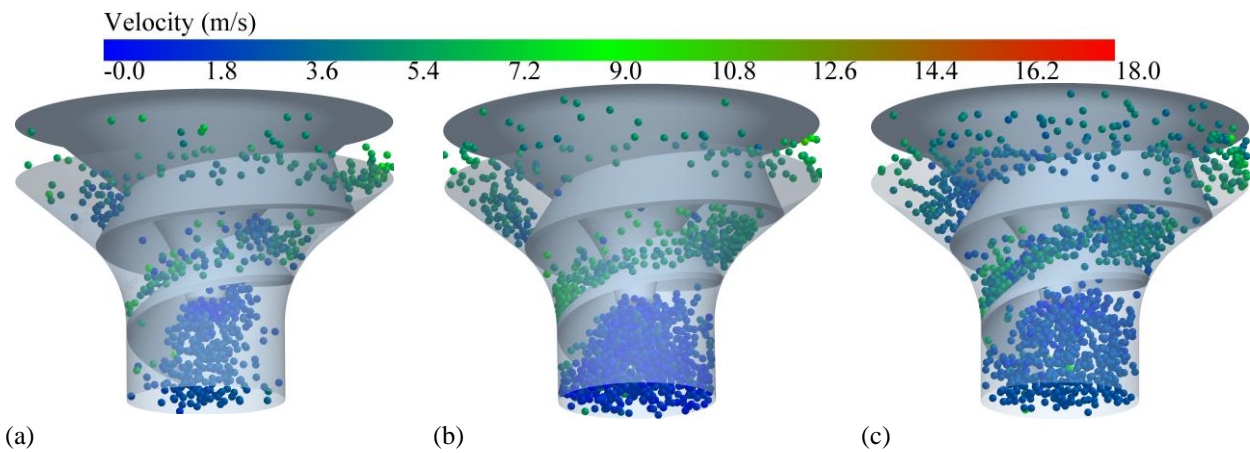


**Fig. 7** Particle distribution in the impeller under  $Q =$  (a) 220, (b) 320, and (c) 420  $\text{m}^3/\text{h}$

design impeller creates a large pressure gradient between the blade pressure side and the suction side. This pressure difference drives the fluid on both sides of the blade, causing high-pressure fluid to leak through the gaps in the shroud to the suction side. Prewhirl and leakage flow impacted the mainstream throughput capacity in the impeller channel, while also influencing the particle movement behaviors.

At a flow rate of 220  $\text{m}^3/\text{h}$ , the inlet pipe wall exhibited a high-speed reverse flow with a screw-like pattern (Fig. 5(a)). This flow rotated in the same direction as the impeller, resulting in the effective flow area reduction in the inlet pipe. The intensity and impact range of this reflux fluctuate periodically with the impeller rotation (Deng et al., 2015); reflux and mainstream are mixed in the middle of the pipeline to achieve equilibrium, a shear vortex structure with opposite internal and external flow directions should be formed near the inlet of the impeller in the inlet pipeline, which causes particles to be deposited in the middle of the inlet pipe. Particles near the inlet pipe wall accelerated from 1.8 to 6 m/s due to reflux entrainment. The remaining particles aggregated towards the pipe center under the influence of the impeller prewhirl and backflow, forming a columnar distribution. The particles in the deposition area rotate clockwise, in the

same direction as the impeller rotation (Li et al., 2024), from the center of the inlet pipeline into the impeller channel and then collision with the hub of impeller. In Fig. 5(b), when the flow rate was increased to  $Q = 320 \text{ m}^3/\text{h}$ , the deposition position moved up to near the impeller head, and the deposited particles were distributed in the pipeline in the shape of "D". As the mixed mining inlet velocity increased, the fluid prewhirl intensity at the impeller front decreased (Fig. 5(c) and Fig. 6(c)), and the particles deposition in the inlet pipeline and the head of the impeller dissipate, and then enter the impeller channel smoothly.

### 3.2 Characteristics of particle distribution in the impeller flow channel

In the impeller channel, the motion of the fluid and particles accelerated as screw type under the influence of impeller blade. Part of the particles and the high-speed rotation of the blade head of the violent impact, causing sudden changes in particle velocity, with the maximum velocity change reaching 14 m/s (Fig. 7). At the impeller head, most particles moved along the pressure side of the impeller, with increasing velocities due to the propulsion effect of the screw blades, with the blade wrap angle and wheel hub diameter increased, the mixed flow velocity further improved and the particles gradually deflected towards the center of the flow channel. In the large wrap

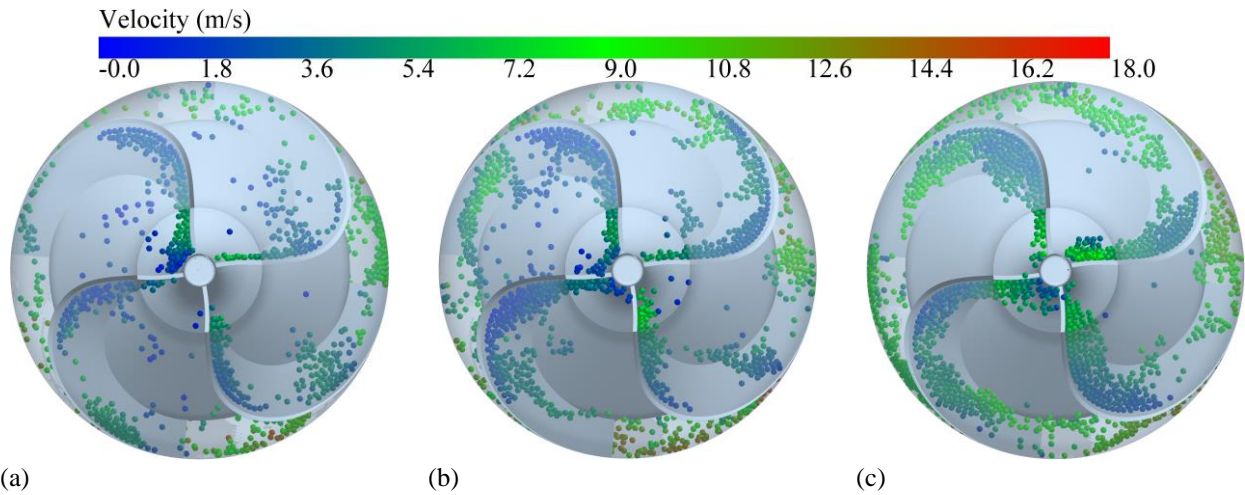


**Fig. 8 Particle distribution in the diffuser under  $Q =$  (a) 220, (b) 320, and (c) 420 m<sup>3</sup>/h**

angle open flow channel, centrifugal force drove the particles towards the impeller outlet, from where they entered the diffuser through the transition flow channel. A small portion of low-velocity particles scattered near the root of the pressure side and exited the impeller flow channel, propelled by the blades.

### 3.3 Characteristics of Particle Distribution in the Diffuser and Outlet Pipe

In the diffuser channel. The particles enter the diffuser mainly along the diffuser shroud cover and the pressure side (Fig. 8(a - c)), exhibiting a non-uniform distribution in the diffuser flow channel, the particle velocity decreased rapidly due to friction and collisions with both the wall and other particles, and gather on the pressure side of the diffuser resulting in more obvious velocity stratification, causing particle energy dissipation. Consequently, particles exhibited longer retention times in the diffuser, increasing the likelihood of accumulation and potential clogging during the conveying process. Furthermore, particles collided with the shaft tube as they exited the diffuser. The tailspin effect of the fluid at the diffuser exits subsequently dispersed the particles uniformly throughout the exit pipeline.

Particle distribution in the diffuser was compared under different flow rates; as the pump flow rate varied, the particles were transported in the diffuser in a better situation, and motion patterns were similar; no clogging of the flow channels due to large-scale particle aggregation occurred. As the pump flow rate increased, the particle distribution in the various flow channels of the diffuser demonstrated an upward trend; on the pressure side of the diffuser, particles converged to form thicker bundles and velocity attenuation was more pronounced; in the outlet pipe, the distribution of the particles was more uniform.

## 4. CHARACTERISTICS OF DYNAMIC NON-UNIFORM FLOW OF PARTICLES

### 4.1 Change in the Number of Particles in the Pump

Figure 9 illustrates the variation in particle count within the pump under different flow rates. In order to reduce the calculation error caused by the simulation time

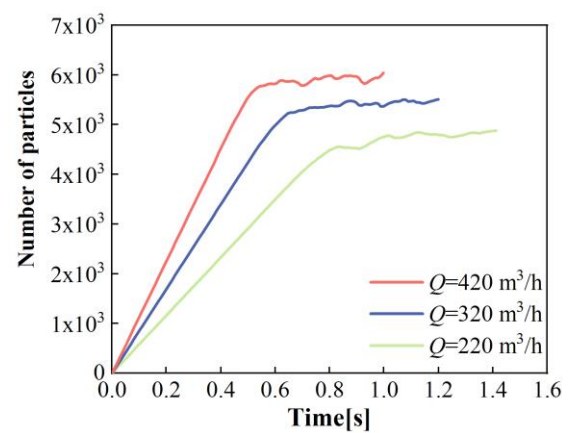
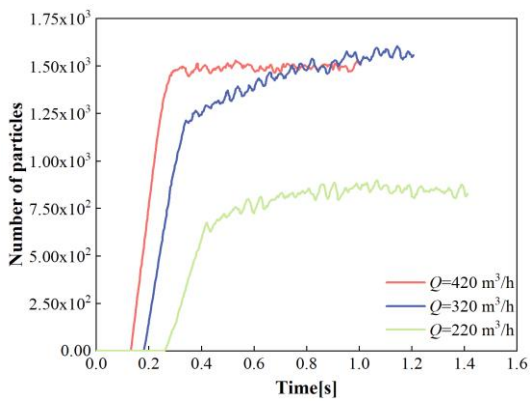


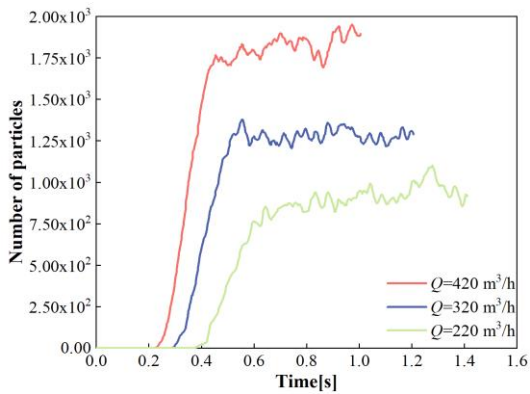
**Fig. 9 Changes in the number of particles within the pump under different flow rates**

and improve the reliability of the analyzed data, the data of 10 operating cycles were used after the number of particles in the pump had reached a stable delivery state as the analysis object. The trend in particle count remained consistent across various flow rates (Fig. 9), and the transportation process could be divided into a growth and stable stage. During the initial pump operation, the particle counts continuously increased with a constant slope before gradually decreasing. At this time, the suction particles at the pump inlet and the discharge particles at the outlet achieved equilibrium. The particle count in the pump approached saturation, and the transport state stabilized, entering a steady period.

After the particle transport pattern tends to be stable, the curve remains fluctuates within a certain range, and the degree of oscillation reflects the non-uniformity of particles passing through the pump. Excessive non-uniformity flow can cause unbalanced radial force on the impeller surface, potentially leading to periodic fatigue deformation of the transmission shaft. This phenomenon significantly impacts the reliability and lifespan of mining pumps (Cheng et al., 2023). Consequently, analyzing the uniformity of particles passing through the main components of the pump is particularly crucial.



(a)



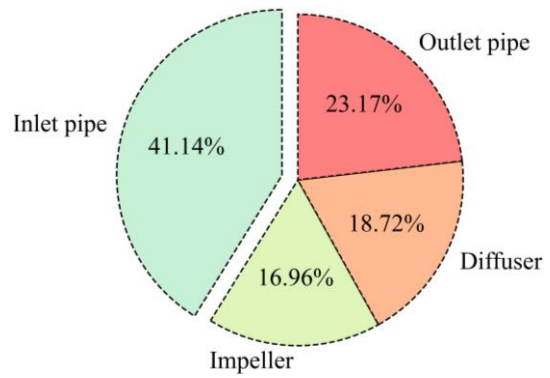
(b)

**Fig. 10** Changes in the number of particles in the (a) impeller and (b) diffuser under different flow rates

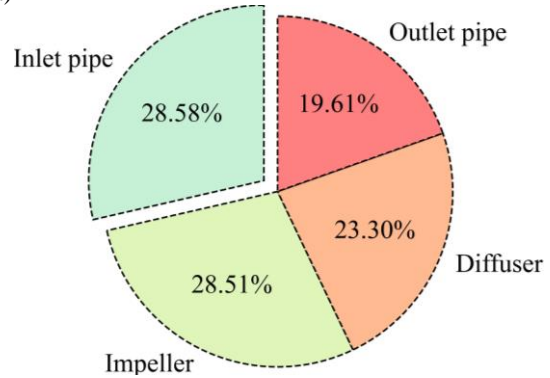
#### 4.2 Change in the Number of Particles in the Impeller-Diffuser

Figure 10 displays the curves of the number of particles passing through the main overflow components. The number of particles in the impeller and diffuser exhibited comparable trends. During the growth phase, the particle quantity in the flow channel increased linearly with a consistent slope, while during the stable phase, it fluctuated in a sawtooth-like pattern. For  $Q = 220$  and  $320$   $m^3/h$ , affected by particle deposition near the impeller head, the particles required longer running time to reach the stable phase in the impeller and diffuser. This corresponds to the columnar particle flow and the formation of the "D"-shaped deposition (Fig. 5 (a) and (b)), and indicates that particle deposition was stable. It did not progress further into subsequent channels with time.

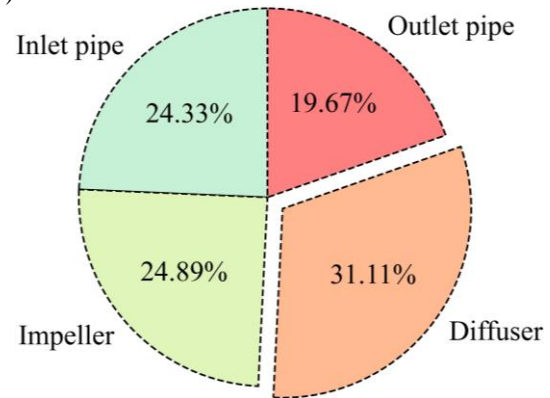
A comparative analysis of the percentage change in particle quantity for each pump component under varying flow rates revealed an inverse correlation between the particle percentage in the inlet pipe and the flow rate (Fig. 11). Notably, for  $Q = 220$   $m^3/h$ , the percentage of particle quantity in the inlet pipe reached a maximum of 41.14%. The main reason was that the inlet backflow caused particles to be deposited in the inlet pipe, resulting in a higher percentage of particulate particle counts than in other flows.



(a)



(b)



(c)

**Fig. 11** Particle percentage in each overflow component of the pump at  $Q =$  (a) 220, (b) 320, and (c) 420  $m^3/h$

The particle percentage in the diffuser demonstrated a positive correlation with the flow rate. For  $Q = 220$  and  $420$   $m^3/h$ , the particle percentage in the diffuser exceeded that in the impeller channel. This indicates that in the same operational period, when particles flowing from the impeller channel pass through the diffuser channel, particle velocity decreases due to particle-particle and particle-wall interactions. Consequently, the time for the particles flowing from the impeller channel to reach the outlet pipe after passing through the diffuser was lagged, resulting in a reduced diffuser flow capacity. However, for  $Q = 320$   $m^3/h$ , the percentage of the particles in both the inlet pipe and impeller channel surpassed 28.0%, with the number of particles in the impeller channel reaching 1539, i.e., 1.81 and 1.03 times that observed at  $Q = 220$  and  $420$   $m^3/h$ , respectively. The main reason was that when  $Q = 220$   $m^3/h$  increases to  $Q = 320$   $m^3/h$ , the influence range of the inlet prewhirl and backflow was reduced, which caused the

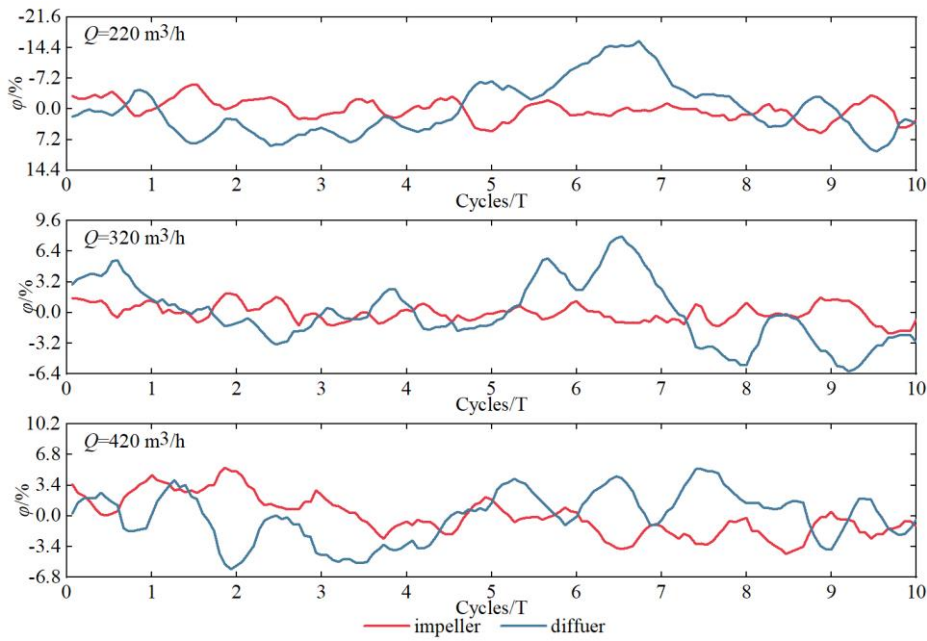


**Fig. 12 Particle quantity non-uniformity in the impeller and diffusers**

particle deposition position to change, which resulted in the increase of the particle quantity in the inlet pipe and impeller channel at  $Q = 320 \text{ m}^3/\text{h}$ .

### 4.3 Non-Uniform Flow of Particles in Impeller-Diffuser

In order to further quantitatively analyze the non-uniform flow characteristics of particles within the impeller and diffuser, defining the non-uniformity of particle flow  $\varphi$ , the calculation formula is as follows:

$$\varphi = \left(1 - \frac{N}{N_{avg}}\right) * 100\% \quad (7)$$

Where:  $N$  is the total number of particles in the impeller or diffuser channel at each time node during the operating cycle.  $N_{avg}$  is the average of the number of particles in the impeller or diffuser at all time nodes.

The variation of  $\varphi$  values within the impeller and diffusers revealed that particle flow in the pump channel exhibited a dynamic non-uniformity (Fig. 12). In the impeller, the positive and negative deviations of the extreme values of particle non-uniformity exceeded 4%. The non-uniformity of the number of particles in the diffuser was disordered, with extreme value positive and negative deviation was larger than the impeller flow channel, and the maximum extreme value deviation appears in  $Q = 220 \text{ m}^3/\text{h}$ , reaching 10% and -16%, respectively. This phenomenon can be attributed to the diffuser completing the media collection along with the conversion of energy, at below design conditions, the fluid flow in the diffuser was more turbulent than at design conditions. Consequently, the non-uniformity deviation in particle distribution became more pronounced.

To quantify the extent of dispersion of the particle non-uniformity  $\varphi$  value within the impeller and the diffuser, the standard deviation of the  $\varphi$  value,  $\sigma$ , is defined, which was calculated as follows:

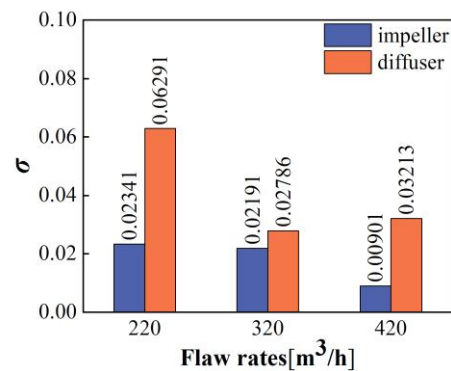


**Fig. 13 Standard deviation of  $\varphi$  value in the impeller and diffusers channels**

$$\sigma = \sqrt{\frac{\sum_{i=1}^n (x_i - \bar{x})^2}{n}} \quad (8)$$

Where:  $x_i$  is the non-uniformity of particles in the impeller/diffuser channel at each time node during the operation cycle, and  $\bar{x}$  is the average value of non-uniformity of particles in the impeller/diffuser channel at all time nodes.

Figure 13 gives the distribution of  $\sigma$  within the impeller and diffuser at various flow rates. The phenomenon of non-uniform flow of particles in the diffuser was greater than the impeller channel. As the flow rate increased, the  $\sigma$  of the  $\varphi$  value of particles in both the impeller and diffuser flow channels gradually decreased, indicating that the phenomenon of non-uniform flow of particles in the impeller channel and the diffuser was gradually weakened. In conjunction with Fig.12, the change in particle flow non-uniformity in the impeller flow channel exhibited a more prominent cyclical pattern with

the increasing flow rate. Concurrently, the non-uniform particle flow in the diffuser also showed improvements.

## 5. CONCLUSION

This study introduces a novel deep-sea mining pump design combining a screw mixed-flow impeller and diffuser. This approach aims to address the challenges of limited coarse particle flow capacity and frequent blockages associated with conventional deep-sea mining pumps. A series of numerical simulations utilizing CFD-DEM coupled computation is employed to evaluate the pump's overflow capacity when transporting 10 mm spherical particles under varying flow rates. The primary conclusions of the study are detailed as follows:

(1) The pump demonstrated excellent particle transportation capabilities across various flow rates, exhibiting no significant clogging behavior. Under design conditions, particles steadily accumulate in diverse formations within the inlet pipe. The particle distribution patterns in the impeller and diffuser remain consistent, though particles are unevenly dispersed across individual diffuser flow channels.

(2) The particle transport state within the pump can be categorized into distinct growth and stability phases. The fluctuation in particle quantity within both the impeller and diffuser follows a consistent pattern. Under low flow conditions, particles require an extended period to reach the stable phase.

(3) During pump operation under diverse flow conditions, the percentage of particles in each component was not equal. The number of particles in the inlet pipeline was negatively correlated with the flow rate, while the diffuser was positively correlated with the flow rate.

(4) Particle flow in the screw mixed-flow deep-sea mining pump displays significant dynamic non-uniformity. The periodic flow of particles is more pronounced in the impeller than in the diffuser. The intensity of non-uniform particle flow exhibits an inverse relationship with the flow rate.

## ACKNOWLEDGEMENTS

The work was supported by the National Natural Science Foundation of China (Grant No.52369018), the Natural Science Foundation of Gansu Province (Grant No.22JR5RA249), and supported by the Gansu Province Higher Education Innovation Foundation (Grant No. 2022A2022), Hongliu Excellent Youth Talent Support Plan of Lanzhou University of Technology.

## CONFLICT OF INTEREST

The authors declare that they have no known competing financial interests or personal relationships that could have appeared to influence the work reported in this paper.

## AUTHORS CONTRIBUTION

**Dengxue Ma:** Writing – original draft, Visualization, Methodology, Data curation, Conceptualization. **Zhengjing Shen:** Conceptualization, Data curation, Methodology, Resources, Supervision. **Wengang Yang:** Investigation, Data curation, Conceptualization. **Fengyi Jiang:** Visualization, Validation, Methodology, Data curation. **Rennian Li:** Resources, Project administration, Funding acquisition.

## REFERENCES

- Cheng, Z., Liu, H., Wang, K., Tan, M., Sun, X., & Shen, D. (2023). Experimental study on unbalanced response characteristics of the impeller of mixed transport pump in deep-sea mining. *Proceedings of the Institution of Mechanical Engineers, Part C: Journal of Mechanical Engineering Science*, 237(6), 1279-1290. <https://doi.org/10.1177/09544062221127125>
- Cundall, P. A., & Hart, R. D. (1985). Development of generalized 2-D and 3-D distinct element programs for modeling jointed rock. Itasca Consulting Group.
- Dehghan, A. A., & Shojaeefard, M. H. (2022). Experimental and numerical optimization of a centrifugal pump volute and its effect on head and hydraulic efficiency at the best efficiency point. *Proceedings of the Institution of Mechanical Engineers, Part C: Journal of Mechanical Engineering Science*, 236(9), 4577-4598. <https://doi.org/10.1177/09544062211056019>
- Dehghan, A. A., Shojaeefard, M. H., & Roshanaei, M. (2024). Exploring a new criterion to determine the onset of cavitation in centrifugal pumps from energy-saving standpoint; experimental and numerical investigation. *Energy*, 293, 130681. <https://doi.org/10.1016/j.energy.2024.130681>
- Deng, L., Hu, Q., Chen, J., Kang, Y., & Liu, S. (2021). Particle distribution and motion in six-stage centrifugal pump by means of slurry experiment and CFD-DEM simulation. *Journal of Marine Science and Engineering*, 9(7), 716. <https://doi.org/10.3390/jmse9070716>
- Deng, Y., Li, R., Han, W., Yang, W., Li, Z., & Zhang, Y. (2015). Characteristics of backflow vortex cavitation in screw centrifugal pump. *Transactions of the Chinese Society of Agricultural Engineering*, 31(1), 86-90. <https://doi.org/10.3969/j.issn.1002-6819.2015.01.013>
- Ding, K., Li, J., Li, C., & Jia, C. (2021). Design and calculation analysis of a slurry transporting pump for deep sea mining. *Ship Engineering*, 43(1), 144-149. <https://doi.org/10.13788/j.cnki.cbgc.2021.01.25>
- Guan, Y., Zou, L., Zheng, H., Bian, Y., & Yu, Z. (2021). Ore particle backflow performance in the deep-sea mining slurry pump. *Journal of Harbin Engineering University*, 42(11), 1557-1565. <https://dx.doi.org/10.11990/jheu.202008008>

- Hu, Q., Chen, J., Deng, L., & Liu, S. (2021). CFD-DEM coupled simulation and experimental study of deep-sea lifting mine pump under extreme working conditions. *The Chinese Journal of Nonferrous Metals*, 31, 2926-2937. <https://doi.org/10.11817/j.ysxb.1004.0609.2021-42074>
- Ji, C., Guan, Y., Zheng, H., & Zhang, H. (2021). Effect of particle size on performance of slurry pump in deep sea mining. *Mining and Metallurgical Engineering*, 41(01),1-6. <https://doi.org/10.3969/j.issn.0253-6099.2021.01.001>
- Kang, Y., Liu, S., Zou, W., Zhao, H., & Hu, X. (2019). Design and analysis of an innovative deep-sea lifting motor pump. *Applied Ocean Research*, 82, 22-31. <https://doi.org/10.1016/j.apor.2018.10.018>
- Kuntz, G. (1979, April). *The technical advantages of submersible motor pumps in deep sea technology and the delivery of manganese nodules*. Off shore Technology Conference (pp. OTC-3367). OTC. <https://doi.org/10.4043/3367-MS>
- Li, R., Ma, D., Shen, Z., Jiang, F., Liu, L., & Han, W. (2024, October). *Study on the inlet backflow characteristics and particle deposition of screw mixed-flow deep-sea mining pump under small flow conditions*. Journal of Physics: Conference Series (Vol. 2854, No. 1, p. 012032). IOP Publishing. <https://doi.org/10.1088/1742-6596/2854/1/012032>
- Shen, Z., & Chu, W. (2018, November). *Effect of particle parameters on erosion wear and performance of screw centrifugal pump*. ASME International Mechanical Engineering Congress and Exposition (Vol. 52101, p. V007T09A018). American Society of Mechanical Engineers. <https://doi.org/10.1115/IMECE2018-88586>
- Shen, Z., Chu, W., & Dong, W. (2018). Effect of particle parameters on flow field and erosion wear characteristics of flow passage components in screw centrifugal pump. *Transactions of the Chinese Society of Agricultural Engineering*, 34(6), 58-66. <https://doi.org/10.11975/j.issn.1002-6819.2018.06.007>
- Su, X., Tang, Z., Li, Y., Zhu, Z., Mianowicz, K., & Balaz, P. (2020). Research of particle motion in a two-stage slurry transport pump for deep-ocean mining by the CFD-DEM method. *Energies*, 13(24), 6711. <https://doi.org/10.3390/en13246711>
- Tram, T. (1991). R&D of Manganese Nodule Mining Systems.
- Wang, G., Huang, Z., Zhou, S., Fu, Q., Zhong, L., Guo, Q., Zhu, D., Liang, D., & Huang C. (2023). Current status and development direction of deep-sea mineral resource exploitation equipment. *Strategic Study of CAE* 2023, 25(06), 1-12. <http://doi.org/10.15302/J-SSCAE-2023.03.001>
- Wang, J., Liu, M., Lei, M., Wu, Q., Wang, K., & Deng, H. (2024). Gas and powder flow characteristics of packed bed: A two-way coupled CFD-DEM study. *International Journal of Multiphase Flow*, 178, 104904. <https://doi.org/10.1016/j.ijmultiphaseflow.2024.104904>
- Wang, R., Guan, Y., Jin, X., Tang, Z., Zhu, Z., & Su, X. (2021). Impact of particle sizes on flow characteristics of slurry pump for deep - sea mining. *Shock and Vibration*, 2021(1), 6684944. <https://doi.org/10.1155/2021/6684944>
- Weaver, D. S., & Mišković, S. (2024). CFD-DEM validation and simulation of gas-liquid-solid three phase high-speed jet flow. *Chemical Engineering Research and Design*, 201, 561-578. <https://doi.org/10.1016/j.cherd.2023.11.046>
- Yakhot, V., & Orszag, S. A. (1986). Renormalization group analysis of turbulence. I. Basic theory. *Journal of Scientific Computing*, 1(1), 3-51. <https://doi.org/10.1007/bf01061452>
- Yang, F. X., Chen, Q., & Zeng, Y. C. (2014). Research on design method of deep-sea mining slurry pump. *Journal of Hefei University of Technology (Natural Science)*, 14(12), 1413-1418. <https://doi.org/10.3969/j.issn.1003-5060.2014.12.002>
- Yang, F., Zhou, Z., Xu, H., & Chen, Q. (2017). Analysis of the influence of rotational speed on solid-liquid two-phase flow of slurry pump for deep-sea mining. *Journal of Hefei University of Technology*, 40(5), 589-594. <https://doi.org/10.3969/j.issn.1003-5060.2017.05.003>
- Yang, H., & Liu, S. (2020). A new lifting pump for deep-sea mining. *Journal of Marine Engineering & Technology*, 19(2), 102-108. <https://doi.org/10.1080/20464177.2019.1709276>
- Yang, J., Liu, L., Lyu, H., & Lin, Z. (2020). Deep-sea mining equipment in China: current status and prospect. *Strategic Study of Chinese Academy of Engineering*, 22(6), 1-9. <https://doi.org/10.15302/J-SSCAE-2020.06.001>
- Zhou, M., Wang, S., Kuang, S., Luo, K., Fan, J., & Yu, A. (2019). CFD-DEM modelling of hydraulic conveying of solid particles in a vertical pipe. *Powder Technology*, 354, 893-905. <https://doi.org/10.1016/j.powtec.2019.07.015>
- Zhu, W., Ma, X. K., Xie, B. Q., & Ma, W. B. (2024). Analysis of the thermo-hydro-mechanical coupled dynamic response of sediments under eccentric driving of deep-sea mining vehicle. *Computers and Geotechnics*, 171, 106389. <https://doi.org/10.1016/j.compgeo.2024.106389>
- Zou, W., Li, H. & Kang, Y. (2021). Research on slurry pump hydraulic lift system for marine mineral resources exploitation. *The Chinese Journal of Nonferrous Metals* 31(10), 2953-2962. <https://doi.org/10.11817/j.ysxb.1004.0609.2021-37997>
- Zou, W., Liu, R., & Liu, S. (2019). Study on lifting motor pumps for coarse particle slurry in sea bed

mining. *China Mechanical Engineering*, 30(24), 2939.  
<https://doi.org/10.3969/j.issn.1004-132X.2019.24.006>

Zou, L., Sun J., Sun, Z., Wang, J., & Yu, Z. (2023). Deep-sea mining core technology in Chian current situation and prospects. *Journal of Harbin Engineering University*, 44(05), 708-716.  
<http://dx.doi.org/10.11990/jheu.202204011>

Zou, Z., Zhu, J., Jia, J., Du, Z., Wang, Q., Zhu, Q., & Li, H. (2020). CFD Simulation of a fluid–solid non-catalytic reaction based on a structure-based mass transfer model: shrinking spherical reaction. *Industrial & Engineering Chemistry Research*, 59(45), 19989-19998.  
<https://doi.org/10.1021/acs.iecr.0c04409>